The Planck clusters in the LOFAR sky: V. LoTSS-DR2: Mass-radio halo power correlation at low frequency

Cuciti, V.; Cassano, R.; Sereno, M.; Brunetti, G.; Botteon, A.; Shimwell, T.W.; ... ; Röttgering, H.J.A.

A&A 680, A30 (2023)
https://doi.org/10.1051/0004-6361/202346755

Astronomy & Astrophysics

The *Planck* clusters in the LOFAR sky

V. LoTSS-DR2: Mass–radio halo power correlation at low frequency

V. Cuciti[1,2,3], R. Cassano[2], M. Sereno[10,11], G. Brunetti[2], A. Botteon[2], T. W. Shimwell[6,4], L. Bruno[1,2], F. Gastaldello[5], M. Rossetti[5], X. Zhang[7], A. Simionescu[8,4,9], M. Brüggen[3], R. J. van Weeren[4], A. Jones[3], H. Akamatsu[8], A. Bonafede[1,2], F. De Gasperin[2,3], G. Di Gennaro[3], T. Pasini[2], and H. J. A. Röttgering[4]

[1] Dipartimento di Fisica e Astronomia, Università di Bologna, Via P. Gobetti 93/2, 40129 Bologna, Italy
e-mail: virginia.cuciti@unibo.it
[2] INAF – IRA, Via P. Gobetti 101, 40129 Bologna, Italy
[3] Hamburger Sternwarte, Universität Hamburg, Gojenbergsweg 112, 21029 Hamburg, Germany
[4] Leiden Observatory, Leiden University, PO Box 9513, 2300 RA Leiden, The Netherlands
[5] INAF – IASF Milano, Via A. Corti 12, 20133 Milano, Italy
[6] ASTRON, the Netherlands Institute for Radio Astronomy, Postbus 2, 7990 AA Dwingeloo, The Netherlands
[7] Max Planck Institute for Extraterrestrial Physics, Giessenbachstrasse 1, 85748 Garching, Germany
[8] SRON Netherlands Institute for Space Research, Niels Bohrweg 4, 2333 CA Leiden, The Netherlands
[9] Kavli Institute for the Physics and Mathematics of the Universe, The University of Tokyo, Kashiwa, Chiba 277-8583, Japan
[10] INAF – Osservatorio di Astrofisica e Scienza dello Spazio, Via P. Gobetti 93/3, 40129 Bologna, Italy
[11] INFN, Sezione di Bologna, Viale Berti Pichat 6/2, 40127 Bologna, Italy

Received 26 April 2023 / Accepted 2 October 2023

ABSTRACT

Context. Many galaxy clusters show diffuse cluster-scale emission in the form of radio halos, showing that magnetic fields and relativistic electrons are mixed in with the intracluster medium. There is in general agreement with the idea that the origin of radio halos is connected to turbulence generated during cluster mergers. Statistical studies of large samples of galaxy clusters in the radio band have the potential to unveil the connection between the properties of radio halos and the mass and dynamics of the host clusters.
Aims. Previous studies were limited to massive clusters and were based on a small number of radio halos. The aim of this paper is to investigate the scaling relation between the radio power of radio halos and the mass of the host clusters at low frequencies and down to lower cluster masses.
Methods. We analysed the clusters from the second catalogue of *Planck* Sunyaev–Zel'dovich sources that lie within the 5634 deg^2 covered by the second Data Release of the LOFAR Two-meter Sky Survey. We derived the correlation between radio power and host cluster mass, and investigated the distribution of clusters without radio halos with respect to this correlation. We used X-ray observations to classify the dynamical state of clusters and investigated its effect on the power of radio halos.
Results. Using different fitting methods, we found a correlation between the power of a radio halo at 150 MHz and the mass of its host cluster down to $3 \times 10^{14}\ M_{\odot}$. For comparison with previous works, with the Bivariate Correlated Errors and intrinsic Scatter (BCES) $Y|X$ method, we obtained the slope of the correlation $B = 3.55 \pm 0.60$ and the normalisation $A = 1.1 \pm 0.1$. This correlation has a large scatter, part of which can be attributed to the different dynamical states of host clusters. We used two statistical tests to show that the distribution of clusters with and without (upper limits) radio halos in the mass–radio power diagram is not compatible with a single correlation and that it is also not compatible with clusters being uniformly distributed below the correlation.

Key words. radiation mechanisms: non-thermal – galaxies: clusters: intracluster medium – galaxies: clusters: general – radio continuum: general – X-rays: galaxies: clusters – acceleration of particles

1. Introduction

Mergers between galaxy clusters are the final stages of cosmic structure formation and are the most energetic events in the current Universe, releasing up to $\sim 10^{63}$ ergs on gigayear timescales. During these events, shocks and turbulence are released into the intracluster medium (ICM), which amplify cluster magnetic fields and accelerate particles to relativistic speeds. Radiation from these non-thermal phenomena in galaxy clusters is observable in the radio band in the form of radio halos and radio relics (e.g. van Weeren et al. 2019, for an observational review). Radio halos are found at the centres of clusters and their emission roughly follows the X-ray emission from the thermal ICM. Radio relics, on the other hand, are located at the periphery of clusters and have elongated morphologies. The currently accepted theoretical picture is that radio halos are powered by turbulence, whereas radio relics trace shock waves propagating through the ICM (Brunetti & Jones 2014, for a theoretical review). Both radio halos and relics are therefore probes of the dissipation of the gravitational energy from large to smaller scales.

In this paper, we focus on radio halos. Studying the statistical properties of radio halos in galaxy clusters has become increasingly important in the last decade as it is a powerful tool to unveil the connection and evolution of the non-thermal cluster-scale emission with both cluster dynamics and cluster mass. Such studies can test theoretical models for the origin of radio halos. Previous studies, such as the

Giant Metrewave Radio Telescope (GMRT) radio halos survey (Venturi et al. 2007, 2008) and its extension (Kale et al. 2013, 2015), have revealed a statistical connection between the presence of radio halos and the merging status of the host clusters (Cassano et al. 2010a; Cuciti et al. 2015, 2021a), supporting the idea that mergers play a key role in the formation of radio halos. Moreover, a correlation exists between the radio power of halos and the mass of the host clusters (Basu 2012; Cassano et al. 2013; Cuciti et al. 2021a; Duchesne et al. 2021; van Weeren et al. 2021; George et al. 2021). The upper limits on the radio power of clusters with no diffuse emission populate a different region in the mass–radio power diagram, typically being about a factor of four below the correlation (Cassano et al. 2013; Cuciti et al. 2021a).

According to turbulent reacceleration models, the radio spectra of radio halos should show a cutoff at a frequency that is proportional to the energy available in the merger (Cassano & Brunetti 2005). In particular, the mass of clusters is one of the parameters that sets the energy budget for particle acceleration. Therefore, massive systems undergoing major mergers are expected to form radio halos with a typical spectral index of $\alpha \sim -1.3$ (with $F_\nu \propto \nu^\alpha$) visible up to ~GHz frequencies before rapidly steepening, while less massive systems and minor mergers are expected to generate ultrasteep spectrum radio halos (USSRHs; $\alpha < -1.5$), which are only detectable at ~100 MHz (Cassano et al. 2012). However, historically, these studies were performed at frequencies of ~1 GHz and this limited the number of detections of radio halos and the mass range that could be explored to $M_{500} > 5{-}6 \times 10^{14}\ M_\odot$ (Cuciti et al. 2021a).

In this respect, the LOw Frequency ARray (LOFAR) has enabled observations of galaxy clusters at frequencies of <200 MHz with unprecedented sensitivity and resolution. LOFAR is carrying out sensitive wide-area surveys of the entire Northern Sky at 120−168 MHz and 42−66 MHz in the context of the LOFAR Two-meter Sky Survey (LoTSS; Shimwell et al. 2017) and LOFAR LBA Sky Survey (LoLSS; de Gasperin et al. 2021), respectively. One of the main goals of these surveys is the discovery of diffuse megaparsec-scale radio sources in galaxy clusters, providing large samples suitable for performing statistical studies. Based on turbulent acceleration models, Cassano et al. (2010b) predicted that the LOFAR survey at 150 MHz should detect ~350 radio halos in the Northern Sky. A first step in this direction was made by van Weeren et al. (2021), who analysed the diffuse emission in 26 galaxy clusters selected from the second *Planck* catalogue of Sunyaev–Zel'dovich (SZ) sources (PSZ2; Planck Collaboration XXVII 2016) that lie within the 424 deg^2 of the first LoTSS Data Release (LoTSS-DR1; Shimwell et al. 2019). van Weeren et al. (2021) found eight radio halos, and therefore needed to complement their measurements with literature information in order to study the mass–radio power correlation.

Recently, we started a large project[1] with the aim of studying the statistical properties of the diffuse sources in galaxy clusters at 150 MHz. To this purpose, we selected all the clusters from the second PSZ2 catalogue that have been covered by the second LoTSS Data Release (LoTSS-DR2; Shimwell et al. 2022). In Botteon et al. (2022, Paper I), we present the sample, describe the data analysis, classify the cluster radio sources, and provide the measurements of different quantities. In Bruno et al. (2023, Paper II), we present the procedure and derive the upper limits to the radio power of clusters with undetected diffuse emission. In Zhang et al. (2023, Paper III), we analysed the available X-ray, *Chandra* and/or *XMM-Newton*, archival data to derive the morphological properties and the ICM density perturbations of clusters. In Cassano et al. (2023, Paper IV), we study the occurrence of radio halos as a function of mass and redshift, and the connection between radio halos and the dynamics of clusters, and compare the results with expectations from theoretical models. In Jones et al. (2023, Paper VI), we focus on radio relics and discuss their occurrence and their scaling relations. Here, we present the correlation between the radio power of halos and the masses of the host clusters (Sect. 3), and discuss the scatter of this correlation and the distribution of clusters with and without radio halos (Sects. 4 and 5). Finally, we compare our results to previous work at higher frequencies (Sect. 6).

2. The sample

The PSZ2 catalogue (Planck Collaboration XXVII 2016) contains 1653 SZ-sources detected over the entire sky, of which 309 lie in the LoTSS-DR2 footprint, and 281 out of 309 have been confirmed as clusters and their mass and redshift have been measured. In Paper I, we classified the diffuse radio emission in those clusters by visually inspecting a set of LOFAR images at different resolutions (with and without source subtraction) together with the optical/X-ray overlay images. In order to make this classification objective and reproducible, we used a decision tree that we followed during the inspection of the images to classify the diffuse emission. The radio sources are classified as follows: radio halos (RH) are extended sources that occupy the region where the bulk of the X-ray emission from the ICM is detected; radio relics (RR) are elongated sources whose position is offset from the bulk of the X-ray emission from the ICM; candidate radio halos and candidate radio relics (cRH/cRR) are cases where the diffuse emission has the appearance of a RH or RR, respectively, but the absence of *Chandra* or *XMM-Newton* X-ray observations prevents unequivocal classification; uncertain (U) are sources for which the emission is either significantly affected by calibration and/or subtraction artefacts or sources that do not fall in the categories of RH or RR; no diffuse emission (NDE) sources are those that do not show the presence of diffuse emission that is not associated with AGN; and not applicable (N/A) sources are those for which the image quality is not adequate to properly classify the emission.

The procedure to measure the radio power of radio halos is described in Paper I. Here, we summarise the main steps and refer the reader to Table A.3 of Paper I for the values of $P_{150\,\mathrm{MHz}}$. We used the Halo-Flux Density CAlculator[2] (HALO-FDCA; Boxelaar et al. 2021) to measure the integrated flux density of radio halos. We adopted an exponential profile to fit the surface brightness of radio halos. This model depends on two parameters: the central surface brightness I_0 and the e-folding radius (r_e). As suggested by Murgia et al. (2009), when calculating the HALO-FDCA derived integrated flux densities, we integrated the best-fit models up to a radius of three times the e-folding radius. This choice leads to a flux density that is ~80% of that that would be obtained by integrating the model up to infinity and is motivated by the fact that halos do not extend indefinitely. The k-corrected radio power of the sources at 150 MHz is derived according to the usual formula and assuming a power-law radio spectrum with a spectral index of $\alpha = -1.3$ (see Eq. (5) in Paper I), which is typical of radio halos (e.g. Feretti et al. 2012;

[1] Images, tables, and further information of all targets can be found on the project website https://lofar-surveys.org/planck_dr2.html

[2] https://github.com/JortBox/Halo-FDCA

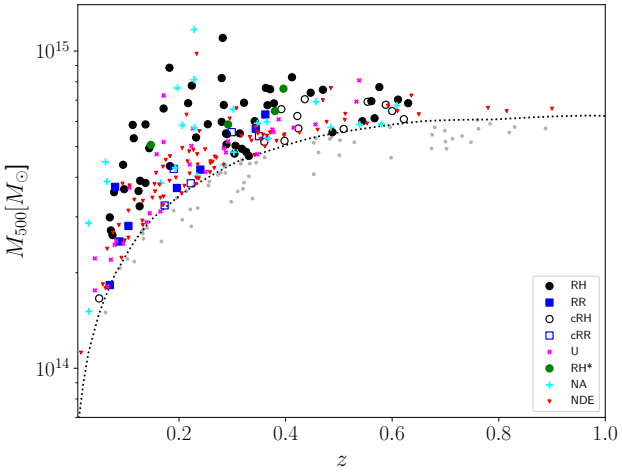

Fig. 1. Mass–redshift distribution of the clusters of the sample. Clusters above the 50% *Planck* completeness line (dotted line) are marked depending on their classification. Grey points represent clusters below the 50% completeness line and are not considered in this paper.

van Weeren et al. 2019). We note that some radio halos may have steeper spectra. The reader should therefore take the values of $P_{150\,\mathrm{MHz}}$ with caution, especially for high-redshift clusters, where the k-correction makes the value of $P_{150\,\mathrm{MHz}}$ more dependent on the adopted α. In a few cases, the fitting could not be performed reliably owing to the low signal to noise of the diffuse emission. These sources are marked RH* and their integrated flux densities cannot be determined accurately with current data.

For 75 of the 114 NDE with available redshift, we derived the upper limit on the radio power of a possible halo by simulating radio halos through the injection of mock visibilities in the LOFAR *uv*-data and assuming negligible flux absorption due to calibration. The injection technique and the resulting upper limits are reported in Paper II.

Here we focus on a subsample of 221 clusters that lie above the 50% *Planck* completeness line (Fig. 1). This means that we may have missed up to 50% of clusters above the completeness line. We do not expect this choice to introduce biases in our results because there are no significant differences between the completeness functions for relaxed and disturbed clusters, as shown by Planck Collaboration XXVII (2016). This choice represents a reasonable compromise between the size and the completeness of the sample. Among these 221 clusters, three are excluded because they lie within the Coma cluster region (which requires a special data reduction scheme given its large angular extent, Bonafede et al. 2021, 2022) and one is PSZ2 G060.10+15.59 for which the ionospheric conditions at the time of the observation did not allow proper direction-dependent calibration, hence it is excluded. Moreover, we do not consider the radio halo in PSZ2 G166.62+42.13 because its emission is contaminated by the emission of multiple radio relics and the radio halo power was not computed for this reason (Botteon et al. 2022). Considering these exclusions, the number of clusters analysed in this paper is 216, we list the number of clusters per category in Table 1.

3. Fitting procedure

The resulting distribution of radio halos in the radio mass–power diagram is shown in Fig. 2 (left). The uncertainties take into account the statistical, systematic, and subtraction error.

Table 1. Number of clusters per category.

	RH	RR	cRH	cRR	RH*	N/A	NDE [(b)]	U
Number	48	20 [(a)]	13	5	4	23	85	30

Notes. [(a)]Twelve of these also host RHs and are counted among the 48 clusters in the RH category. [(b)]We have upper limits for 53 of these clusters (see Paper II).

We refer the reader to Paper I for the estimation of these uncertainties. To derive the parameters of the correlation, we follow the fitting procedure outlined in Cassano et al. (2013) and Cuciti et al. (2021a). Specifically, we adopt the Bivariate Correlated Errors and intrinsic Scatter (BCES) linear regression algorithms (Akritas & Bershady 1996) to fit the observed M_{500}–$P_{150\,\mathrm{MHz}}$ data points with a power law in the form:

$$\log\left(\frac{P_{150\,\mathrm{MHz}}}{10^{24.5}\,\mathrm{W\,Hz^{-1}}}\right) = B\,\log\left(\frac{M_{500}}{10^{14.9}\,M_\odot}\right) + A, \quad (1)$$

where A and B are the intercept and the slope of the correlation, respectively.

Considering $Y = \log(P_{150\,\mathrm{MHz}}) - 24.5$ and $X = \log(M_{500}) - 14.9$, and having N data points (X_i, Y_i) with errors $(\sigma_{X_i}, \sigma_{Y_i})$, we estimate the raw scatter as:

$$\sigma^2_{\mathrm{raw}} = \frac{1}{N-2}\sum_{i=0}^{N} w_i (Y_i - BX_i - A)^2, \quad (2)$$

where

$$w_i = \frac{1/\sigma_i^2}{(1/N)\sum_{i=0}^{N} 1/\sigma_i^2} \quad \text{and} \quad \sigma_i^2 = \sigma_{Y_i}^2 + B^2\sigma_{X_i}^2. \quad (3)$$

To evaluate the 95% confidence region of the correlation, that is, the area that has a 95% probability of containing the "true" regression line, we calculated the 95% confidence interval of the mean value of Y, $\langle Y\rangle$. For a given X, this is $\langle Y\rangle \pm \Delta Y$, where

$$\Delta Y = \pm 1.96\sqrt{\left[\sum_{i=0}^{N}\frac{(Y_i - Y_m)^2}{N-2}\right]\left[\frac{1}{N} + \frac{(X - X_m)^2}{\sum_{i=0}^{N}(X_i - X_m)^2}\right]}, \quad (4)$$

where $Y_m = BX_i + A$ and $X_m = \sum_{i=0}^{N} X_i/N$ for each observed X_i.

The parameters of the correlation were derived considering only clusters with radio halos, and are shown in the top panel of Table 2, together with the results from a 5000 bootstrap resampling analysis. The parameters that we inferred considering also candidate radio halos are listed in the second panel of Table 2. We also report the raw scatter of the correlation, σ_{raw}, and the Spearman correlation coefficient, r_s, which is a measure of the monotonicity of the relationship between two variables. In both cases, we obtained a value of $r_s \sim 0.8$, which means that the correlation is monotonically increasing and the probability that such a correlation is due to chance (p-value) is $<10^{-11}$.

In addition, we derived the parameters of the correlation considering only radio halos with the Bayesian LInear Regression in Astronomy method (LIRA; Sereno 2016). We used a mass distribution that depends on the redshift. The mass distribution of the *Planck* clusters we considered is limited at large masses by the steepness of the halo mass function and at small masses by the adopted 50% mass completeness threshold. These two factors make the distribution approximately lognormal (Lima & Hu 2005). We were then able to model the mass

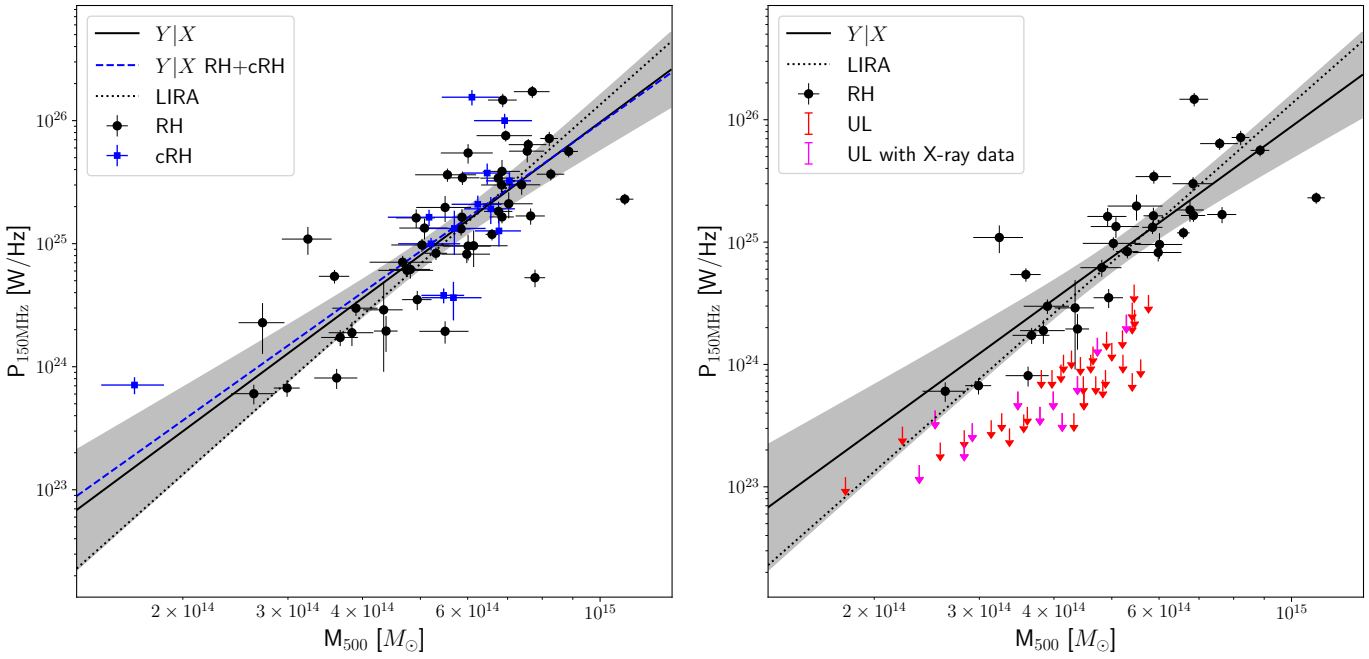

Fig. 2. Mass–radio power diagram. Left: mass–radio power diagram for radio halos (black points) and candidate radio halos (blue squares) above the 50% *Planck* completeness. The solid line and the shadowed region represent the correlation to radio halos only obtained with the BCES $Y|X$ method and the 95% confidence region. The dashed line is the correlation obtained considering also candidate radio halos. The black dotted line is obtained fitting only radio halos with LIRA. Right: mass–radio power diagram for clusters with radio halos and upper limits with $0.06 < z < 0.4$ and $100\,\mathrm{kpc} < r_e < 400\,\mathrm{kpc}$. The solid line and the shadowed region represent the correlation obtained with the BCES $Y|X$ method and the 95% confidence region, while the dotted black line is obtained with LIRA.

Table 2. Fitting parameters.

Method	B	Err B	A	Err A	$\sigma_{\rm raw}$	r_s
Radio halos only						
BCES $Y\|X$	3.59	0.48	1.1	0.09	0.39	0.79
Bootstrap	3.63	0.50	1.1	0.09		
BCES bisector	4.30	0.10	1.2	0.06		
Bootstrap	4.35	0.50	1.2	0.09		
BCES orthogonal	5.24	0.50	1.4	0.1		
Bootstrap	5.37	0.50	1.4	0.1		
LIRA	4.30	0.68	1.2	0.1		
Radio halos and candidate radio halos						
BCES $Y\|X$	3.45	0.44	1.1	0.09	0.39	0.78
Bootstrap	3.55	0.49	1.1	0.09		
BCES bisector	4.19	0.16	1.3	0.05		
Bootstrap	4.28	0.50	1.3	0.09		
BCES orthogonal	5.19	0.69	1.4	0.1		
Bootstrap	5.32	0.71	1.4	0.1		
$0.06 < z < 0.4$ and $100\,\mathrm{kpc} < r_e < 400\,\mathrm{kpc}$						
BCES $Y\|X$	3.55	0.60	1.1	0.1	0.35	0.86
Bootstrap	3.59	0.60	1.1	0.1		
BCES bisector	4.11	0.10	1.2	0.07		
Bootstrap	4.12	0.50	1.2	0.1		
BCES orthogonal	4.79	0.50	1.3	0.1		
Bootstrap	4.81	0.60	1.3	0.1		
LIRA	4.13	0.70	1.2	0.14		

distribution of the observed sample as a lognormal function with redshift-dependent mean and dispersion, which was shown to be a reliable approximation for the *Planck* sample (see Fig. 12 in Sereno & Ettori 2015). Moreover, we considered that both the radio power and the mass have a scatter with respect to a "true" mass, which is unknown. With this approach, we are taking into account the fact that the *Planck* masses derived from the SZ signal are proxies of the "true" mass. In general, we find good agreement between the results of LIRA and BCES. With the assumption that Y and X are both linear proxies of a third variable, the fit is symmetric with respect to Y and X; indeed the LIRA results are very similar to those found with the BCES bisector method.

In Cuciti et al. (2021a), we showed that the regression analysis applied to a sample with a large scatter in radio power can lead to steeper slopes with respect to the "true" underlying slope. This effect is more pronounced for the bisector and orthogonal methods. The scatter in radio power of the sample analysed here is even larger. Hence, among the fitting methods offered by BCES, the $Y|X$ is the most accurate one. On the other hand, LIRA is the only method that allows us to take into account the distribution of clusters in the mass–redshift space. Therefore, in Fig. 2 we show both the BCES $Y|X$ and LIRA methods.

4. Scatter of the correlation

The correlation between the radio power of radio halos at 150 MHz and the mass of the host clusters shows a relatively large scatter (Fig. 2). While measurement errors play a role, there is likely some inherent variation due to the complex mixture of clusters in different dynamical stages and radio halos with different spectra and different sizes (Cuciti et al. 2021a). To ascertain the effect of dynamical status on the scatter of the correlation, similar to Cuciti et al. (2021a), we used the X-ray morphological disturbance as a proxy. This is a single parameter, and is derived from the combination of the concentration

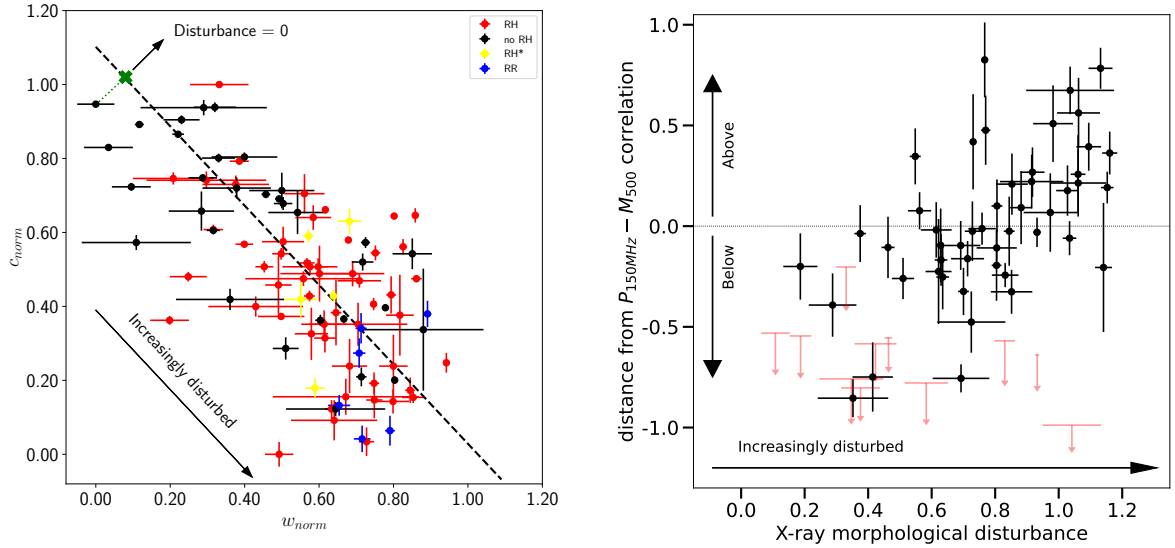

Fig. 3. X-ray morphological disturbance. Left: normalised concentration parameter–centroid shift diagram for all the clusters of the sample with available X-ray observations. The black dashed line is the regression line. The green cross marks the projection on the regression line of the cluster with disturbance = 0. Right: distance of radio halos (black points) and upper limits (red arrows) from the mass–radio power correlation (BCES $Y|X$ method) versus X-ray morphological disturbance.

(c, Santos et al. 2008) and centroid shift (w, Böhringer et al. 2010) parameters.

Among the 309 objects of the total sample of *Planck* clusters in LoTSS-DR2 (see Sect. 2), 143 (46%) have X-ray (*Chandra* or *XMM-Newton*) data. We used these archival data to derive the morphological parameters c and w (Paper III). Here, we adopt a slightly different approach to measure the X-ray morphological disturbance with respect to Cuciti et al. (2021a). We start by normalising the values of each morphological parameter, $\mathcal{P}$, such that

$$\mathcal{P}_{\rm norm} = \frac{\log(\mathcal{P}_i) - \min(\log(\mathcal{P}))}{\max(\log(\mathcal{P})) - \min(\log(\mathcal{P}))}. \quad (5)$$

This allows us to take into account the different ranges of values covered by c and w. We then fit the distribution of $c_{\rm norm}$ versus $w_{\rm norm}$ (Fig. 3, left) with a power law in the form

$$c_{\rm norm} = m \times w_{\rm norm} + q, \quad (6)$$

using the same methods described in Sect. 3. With the BCES bisector method, we obtain $m = -1.07 \pm 0.07$ and $q = 1.1 \pm 0.04$. We derived the projected position of each cluster along the fitting line and we assumed that the cluster with X-ray disturbance = 0 is the first along the line starting from the top left corner of the plot (i.e. high c and low w; see Fig. 3, left). The disturbance of the other clusters is calculated as the distance along the fitting line from the cluster with disturbance = 0. The choice of the zero point is arbitrary, and hence the values of the disturbance do not have a direct physical meaning if not in comparison with the other clusters. With this definition, higher values of the X-ray morphological disturbance indicate clusters that are more dynamically active. We note that with this definition, a cluster with a pronounced core (high c) that is very disturbed on the large scale (high w) would have similar disturbance to a cluster that appears less morphologically disturbed (lower w) but has a disrupted core (lower c).

Figure 3 (right) shows the distance (on the $P_{150\,\rm MHz}$ axis) of radio halos from the mass–radio power correlation versus their X-ray morphological disturbance. We confirm the trend between these two quantities, with radio halos that lie above the correlation being located in more dynamically disturbed clusters. Figure 3 (right) suggests that the merger activity has a key role in determining the position of radio halos with respect to the correlation, inducing at least part of the large scatter. This can be explained by two aspects, or most likely by the combination of them: the different timescales of the mergers and the different types of merger. This is supported by numerical simulations showing that the emission of radio halos increases in the early stages of the merger when turbulence accelerates electrons, and then decreases along with the dissipation of turbulence at later merger stages (Donnert et al. 2013). In particular, in one simulated cluster with $M_{200} = 10^{15}\,M_{\odot}$, Donnert et al. (2013) showed that, in the initial stage of the merger, the radio power increases by a factor of about 30 on a timescale of ∼1.5 Gyr and then decreases by the same factor in less than 1 Gyr. In the mass–radio power plane, this translates into a migration of clusters from the region of the upper limits to the correlation (or above) and a gradual movement back again. On the other hand, the most powerful mergers (high mass ratio and/or small impact parameter) dissipate a larger amount of energy in the ICM and therefore the free energy available for particle acceleration and magnetic field amplification is higher (e.g. Cassano et al. 2016).

In general, it is expected that the clusters for which we derived upper limits on the radio power are less disturbed. Unfortunately, while we have X-ray observations for all the radio halos in the sample analysed in this paper, we only have X-ray data for 11 clusters with radio upper limits. We plot these upper limits in Fig. 3 (right) as red arrows. Although the incompleteness of the X-ray information does not allow us to derive meaningful statistical conclusions (see Paper IV for a deeper discussion on this), it is interesting to note that ∼70% of the upper limits have low X-ray morphological disturbance. We did not find evidence of a relation between the disturbance of the clusters with upper limits and their mass and/or redshift. However, we stress again that larger numbers are necessary to make this kind of consideration. We note that there are three highly disturbed clusters with upper limits (from right to left: PSZ2 G071.63+29.78, PSZ2 G137.74−27.08,

PSZ2 G127.50−30.52). According to turbulent reacceleration models, radio halos should have a typical lifetime of ∼1 Gyr (Brunetti et al. 2009), which is similar to the merger timescale. As turbulence takes some time to cascade from large to small scales, this implies that radio halos evolve from the off to the on state and vice versa, and these phases can span a non-negligible fraction of 1 Gyr. This produces a difference in the timescale of the X-rays and radio properties as an effect of the merger event. Indeed, during these phases, radio halos would appear underluminous or absent, whereas the hosting cluster would appear disturbed in the X-rays. Another possibility is that these clusters host radio halos with extremely steep spectra, which are difficult to detect even at LOFAR HBA frequencies.

In the literature, there are other parameters that combine two morphological estimators, such as c and w (e.g. Rasia et al. 2013; Lovisari et al. 2017; Campitiello et al. 2022; Ghirardini et al. 2022). One of these is the parameter M, first introduced by Rasia et al. (2013) and then used in other works (e.g. Lovisari et al. 2017; Campitiello et al. 2022). To validate our results, in Appendix A we derive M for the clusters of the sample by combining the parameters c and w and compare it with the value of the disturbance. As expected, we find that the two values are very well correlated. This indicates that there is agreement in the classification of the dynamical state of clusters using these two methods. In fact, we show that even considering M to classify the dynamics of clusters, we find evidence that the most disturbed clusters are scattered up with respect to the correlation.

5. Distribution of clusters in the M_{500}−$P_{150\,\mathrm{MHz}}$ diagram

It is known that massive galaxy clusters ($M_{500} > 5{-}6\times10^{14}\,M_\odot$) show a bimodal behaviour in the M_{500}−$P_{1.4\,\mathrm{GHz}}$ diagram, with disturbed clusters populating the correlation and relaxed systems appearing as a separated population with upper limits to their radio power (Cassano et al. 2013; Cuciti et al. 2021a). Here, we investigate whether a similar behaviour is found also at 150 MHz. To this end, we focus on clusters at $0.06 < z < 0.4$ and on radio halos with $100\,\mathrm{kpc} < r_\mathrm{e} < 400\,\mathrm{kpc}$ (Fig. 2, right). In these ranges, we have 32 radio halos and 46 upper limits. In this redshift range, current observations are able to provide stringent upper limits (Paper II). The range of r_e is chosen because upper limits are all placed using $r_\mathrm{e} = 200$ kpc (which is consistent with the mean r_e of radio halos in the sample; see Paper II), and therefore the radio power of radio halos that are more than a factor of two larger or smaller than this value would not be easily comparable with these upper limits. Figure 2 shows that we can now reliably constrain the correlation down to masses of the order of $\sim3\times10^{14}\,M_\odot$, whereas below we do not have sufficient statistics. To study the distribution of clusters with and without radio halos in the M_{500}−$P_{150\,\mathrm{MHz}}$ diagram, we adopt two approaches, which we outline below.

5.1. Akaike information criterion

In this section, we use the Akaike information criterion (AIC; Akaike 1974) to determine if the distribution of clusters in the M_{500}−$P_{150\,\mathrm{MHz}}$ plane is better described with a model composed of two separate populations, one for the radio halos and one for the upper limits, or if it is better described by a single population. The AIC value of each model is calculated as

$$\mathrm{AIC} = 2k - 2\ln(\hat{L}), \tag{7}$$

where k is the number of free parameters of the model and $\hat{L}$ is the maximum value of the likelihood function as a function of the model parameters; see Eq. (8). In general, given a set of models, the preferred model is the one with the minimum AIC value. As opposed to the full LIRA regression analysis adopted in Sect. 3, here we did not consider the scatter of the *Planck* mass with respect to the true mass, and the modelling of the mass distribution. For each scaling relation, there are three fitting parameters, namely the normalisation A, the slope B, and the scatter σ. We assumed that the value for a measurement for which only an upper limit is provided follows a uniform distribution spanning the range from $P_\mathrm{UL} - 1$ to P_UL, where P_UL is the logarithm of the value of the upper limit reported in Paper II. After marginalisation over the unobserved true values Y, the likelihood can be written as

$$L = \prod_i^{N_\mathrm{det}} \frac{1}{\sqrt{2\pi(\sigma_\mathrm{det}^2 + \delta_i^2)}} \exp\left(\frac{(A_\mathrm{det} + B_\mathrm{det}x_i - y_i)^2}{\sigma_\mathrm{det}^2 + \delta_i^2}\right) \times \prod_i^{N_\mathrm{ul}} \frac{\mathrm{erf}\left(\frac{A_\mathrm{ul}+B_\mathrm{ul}x_i-Y_\mathrm{min}}{\sqrt{2}\sigma_\mathrm{ul}}\right) - \mathrm{erf}\left(\frac{A_\mathrm{ul}+B_\mathrm{ul}X_i-Y_\mathrm{max}}{\sqrt{2}\sigma_\mathrm{ul}}\right)}{2(Y_\mathrm{max} - Y_\mathrm{min})}, \tag{8}$$

where x_i and y_i are the measured values of the ith cluster, δ_i is the measurement uncertainty on y_i, erf is the error function, $Y_\mathrm{max} = P_\mathrm{UL}$, and $Y_\mathrm{min} = P_\mathrm{UL} - 1$ (see Appendix B). Uncertainties on the x value are not considered in Eq. (8).

In the first model, we fitted both radio halos and upper limits with a single scaling relation, that is, $A_\mathrm{det} = A_\mathrm{ul}$, $B_\mathrm{det} = B_\mathrm{ul}$, and $\sigma_\mathrm{det} = \sigma_\mathrm{ul}$. In this case, $k = 3$. In the second model, we fitted radio halos and upper limits with two separate scaling relations. In this case, $k = 6$.

We obtained AIC = 150.9 for the first model and AIC = 46.2 for the second. According to the AIC, the model with two separate correlations, that is, one for the radio halos and one for the upper limits, is the one that minimises the information loss and best describes the distribution of clusters in the mass–radio power diagram. On the other hand, the model with just one correlation is $\sim2\times10^{-23}$ times less likely to minimise the information loss than the model with two relations.

To check for agreement between the maximum likelihood analysis based on Eq. (8) and the Bayesian analysis based on LIRA in the case of RHs and ULs following two different relations, we resampled the data 1000 times and fitted each mock data set with LIRA under the same assumptions detailed in Sect. 3. Detected radio halos were extracted from Gaussian distributions centred around the measured value of the radio power and with dispersion equal to the associated uncertainty. The value of each upper limit was extracted from a uniform distribution spanning the range from $P_\mathrm{UL} - 1$ to P_UL. Each sampled population was fitted with LIRA under the regression scheme detailed in Sect. 3. Posterior distributions were obtained by putting together the mean estimated values of the marginalised distributions of each fitted sample. The best-fit values from the maximum likelihood analysis are in full agreement with the Bayesian analysis exploiting LIRA (Sect. 3).

5.2. Monte Carlo test

In this section, we explore the distribution of clusters around the mass–radio power correlation. In Fig. 4 we show the distribution

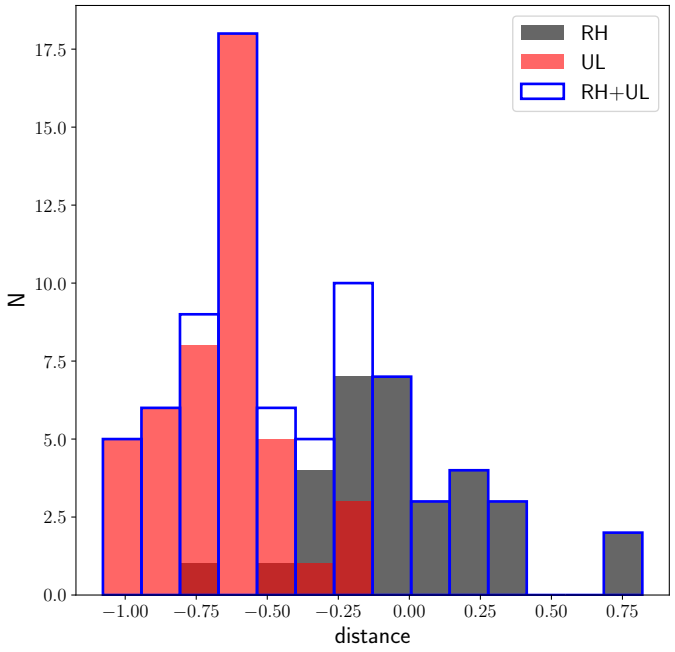

Fig. 4. Distribution of distances of radio halos (black) and upper limits (red) from the correlation shown in Fig. 2 (right). The sum of upper limits and radio halos in each bin is given by the blue histogram.

of the distance along the $P_{150\,\mathrm{MHz}}$ axis of radio halos and upper limits from the correlation shown in Fig. 2 (right). We note that radio halos and upper limits exhibit a bimodal distribution, albeit with some overlapping distances. Here, we test whether the distances shown in Fig. 4 are compatible with clusters being normally distributed above the correlation and uniformly distributed below the correlation. We note that we cannot exclude that the peak of the distribution of the upper limits is driven by the sensitivity limit of our observations. The distribution of the radio power of clusters that currently have an upper limit may be broader and may extend to much larger distances from the correlation. The peak of the distribution of the radio halos is instead attributed to the fact that clusters with radio halos follow the correlation and are distributed around it with a certain scatter. In this view, the correlation represents a region of the diagram that is more densely populated than the rest.

Another possibility, which we test and exclude in the following, is that the mass–radio power diagram is uniformly populated and the correlation is merely a result of sensitivity limitations. In that case, the apparent correlation would only follow the upper envelope of the powers of radio halos, while the less powerful halos would fall below the sensitivity limit of our observations. This data censoring would decrease the number of radio halos below the correlation (the left hand side of the black distribution in Fig. 4). We point out that this scenario does not hold for clusters with $M_{500} > 5.5\times10^{14}\,M_{\odot}$, because at those masses we have only clearly detected radio halos and no upper limits[3]. This does not mean that 100% of the high-mass clusters of the total sample (Paper I) have a radio halo, because here we are not considering clusters with RR only, U cases, or NDE clusters without an available upper limit. We refer the reader to Paper IV for a discussion on the fraction of clusters with radio halos as a function of mass.

[3] The clusters for which we were not able to derive a meaningful upper limit are uniformly distributed in mass (Paper II), and so this incapability cannot be due to the missing upper limits.

To perform this test, we used a Monte Carlo approach. Upper limits seem to have a trend in radio power versus mass. This trend is mainly driven by the fact that the clusters at the highest redshifts are also among the most massive ones, and even if the upper limits are similar in terms of flux density to the lower redshift ones, their radio power is higher. As a first step, we evaluate this correlation in the form $\log(P_{\mathrm{UL}}) = m \times \log(M_{\mathrm{UL}}) + q$. We obtained $m = 2.66$ and $q = -14.9$, with a scatter $\sigma_{\mathrm{raw}} = 0.2$ dex estimated as in Eq. (2). In our sample, we have 78 clusters with $0.06 < z < 0.4$ that have either a radio halo with $100\,\mathrm{kpc} < r_{\mathrm{e}} < 400\,\mathrm{kpc}$ (32) or an available upper limit (46). We started generating 78 clusters with random masses, with the requirement that the distribution of masses resembles the one we have in the sample. To do so, we divided the mass range into three bins, and in each bin we placed the same number of clusters that we have in the sample. We assign a radio power to these clusters so that they are distributed according to the radio halo correlation in the M_{500}–$P_{150\,\mathrm{MHz}}$ diagram. We then added a random value – extracted from one of the probability density functions (PDFs) shown in Fig. 5 – to each radio power. The zero point on the X-axis of Fig. 5 (left) represents the correlation. If a negative value of X (on the left of the zero point) is randomly extracted, the cluster gets shifted below the correlation, and if a positive value of X is randomly extracted then the cluster gets shifted above the correlation. Around the correlation, clusters are normally distributed with $\sigma = \sigma_{\mathrm{raw}} = 0.35$ dex. Below the correlation, clusters are uniformly distributed. The different PDFs shown in Fig. 5 (left) correspond to different "cuts"; that is, different distances from the correlation where the uniform distribution starts. In this formalism, cut = −0.0 means that clusters are uniformly distributed from the correlation down, and cut = −0.1 means that clusters are normally distributed until 0.1 dex below the correlation and then they are uniformly distributed further below.

Given this initial random distribution on the M_{500}–$P_{150\,\mathrm{MHz}}$ diagram, we decide whether a cluster is classified as radio halo or upper limit based on its position: if it is above the upper limits correlation, then it is a radio halo; otherwise, it is an upper limit. We define how far below the correlation clusters can be distributed by imposing that the numbers of radio halos and upper limits in the simulation are similar to those in the sample (32 radio halos and 46 upper limits). This sets the lower limit to the left of the PDFs in Fig. 5 (left). As the upper limits distribution represents our observational limit, when a cluster is classified as an upper limit, we assign a random value to its radio power within the scatter of the upper limits correlation. This is to take into account the fact that there is some scatter in the values of upper limits related to the quality of the images, the presence of bright sources in the field, and the cluster redshift, and therefore some upper limits lie above and some below the upper limits correlation.

We repeated this procedure 10 000 times and computed the radio halo correlation each time. The mass–radio power diagram resulting from one of the runs with cut = 0.0 is shown in Fig. 5 (right) as an example. We evaluated the probability that, over the 10 000 Monte Carlo runs, the fraction of radio halos falling within the scatter of the upper limits correlation is smaller than the one we measure in the sample (0.03); or, in other words, the probability that radio halos and upper limits are more separated than in the sample. We list the obtained probabilities for each cut in Table 3.

These results suggest that the probability that the observed distribution of radio halos and upper limits in the mass–radio power diagram is due to our sensitivity limit applied to a

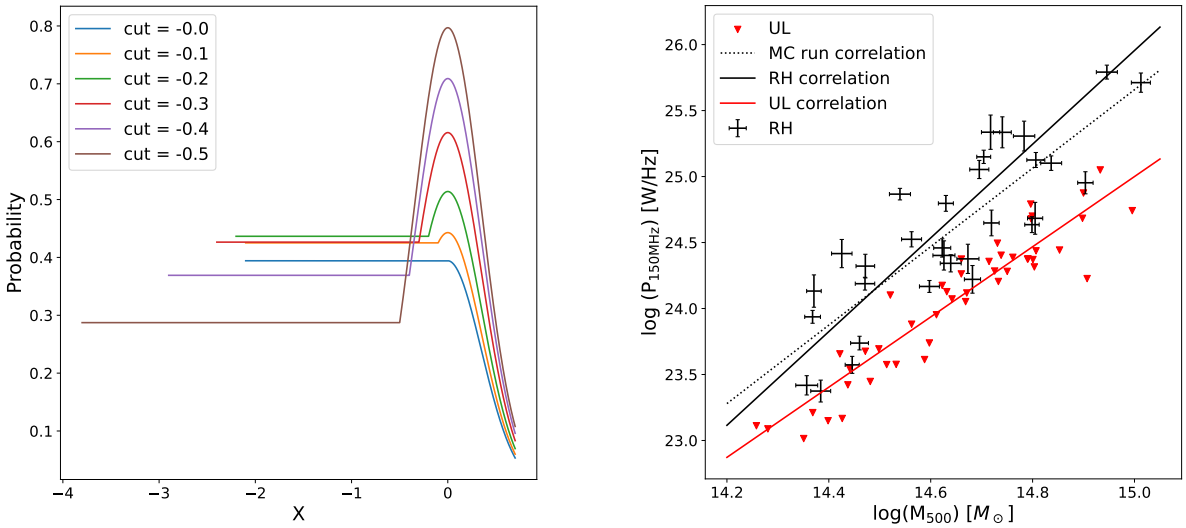

Fig. 5. Monte Carlo test. Left: PDFs with different cuts. PDFs are normalised so that the area below each curve corresponds to 1. We used these PDFs to randomly extract values to add to the radio power of halos on the correlation and distributed them on the M–P plane. Right: example random distribution of clusters in the mass–radio power diagram. Errorbars are radio halos, arrows are upper limits. The black and red solid lines represent the radio halo and upper limits correlation we find in the sample, respectively.

Table 3. Results of Monte Carlo test.

Cut	Probability
−0.0	0.30%
−0.1	0.33%
−0.2	0.57%
−0.3	1.02%
−0.4	2.30%
−0.5	4.65%

uniform distribution of clusters starting below an upper envelope (cut = 0.0) is <0.3%. This probability is still <5% when the uniform distribution starts three times below the correlation (cut = −0.5). This means that the correlation we observe in our sample is indeed a more densely populated region of the M_{500}−$P_{150\,\mathrm{MHz}}$ diagram and that the decrease in the number of radio halos below the correlation in Fig. 4 is not simply due to the sensitivity limit of our observations. In addition to this, we stress again that the distribution of massive clusters in the test (e.g. Fig. 5, right) is significantly different from what we see in the sample (Fig. 2, right), where all clusters with $M_{500} > 5.5 \times 10^{14}\,M_{\odot}$ host radio halos.

6. Comparison with high-frequency samples

In Fig. 6, we show a comparison between the sample that we analysed here and previous studies. On the left panel, we highlight the radio halos of the LOFAR DR2 *Planck* sample that were already reported in the literature (black points). The number of radio halos is now almost two times larger than in previous studies and almost three times larger if we also consider candidate radio halos. Specifically, among the 48 confirmed radio halos analysed in this paper, 20 are new discoveries. The majority of the new detections are located at masses below $5 \times 10^{14}\,M_{\odot}$. At these masses, turbulent reacceleration models predict that a large fraction of clusters should host USSRHs (Paper IV). However, the available observations at higher frequencies do not allow us to test this expectation. In fact, for most of the low-mass clusters of the sample, the expected flux density at 610 MHz with $\alpha = -1.3$ would be comparable to the typical upper limits found with the GMRT at those frequencies (Venturi et al. 2008; Kale et al. 2015; Cuciti et al. 2021b). In this respect, we have recently been allotted uGMRT observations (PI: R. Cassano) of the radio halos discovered with LOFAR, which will be 5−10 times more sensitive than those used in Cuciti et al. (2021b) and will allow us to detect radio halos with spectra as steep as $\alpha \sim -1.5$–2.

In the right panel of Fig. 6, we show both radio halos and upper limits from the LOFAR DR2 *Planck* sample together with those from the sample analysed in Cuciti et al. (2021b), which, until now, was the largest complete sample of clusters with deep radio observations at frequencies larger than 600 MHz. We plot both radio halos and USSRH (and candidate USSRHs) from the GMRT sample. For consistency, we also plot the correlation derived for radio halos plus USSRHs for the statistical sample (see Table 1 in Cuciti et al. 2021b). We note that the correlation in Cuciti et al. (2021a) was derived at 1.4 GHz. We assumed a spectral index of $\alpha = -1.3$. The right panel of Fig. 6 shows that we can now investigate the correlation and the position of the upper limits with respect to the correlation in a much larger mass range that was previously inaccessible. In spite of the low statistics and relatively small mass range of the high-frequency sample, we note that the correlation found at 150 MHz is well in line with the extrapolation of the correlation derived at 1.4 GHz, also in the low-mass regime. From a theoretical point of view, the scatter of the correlation is expected to increase at low frequencies because of the intervening population of USSRHs, which are less luminous than classical radio halos (Cassano 2010). Compared to the correlation derived in Cuciti et al. (2021a) at 1.4 GHz, which has a scatter of ∼0.3 dex, at 150 MHz we find a larger scatter (∼0.4).

Not only has the number of radio halos dramatically increased, but so has the number of available upper limits. Most importantly, the upper limits derived with LOFAR are deeper than those derived at higher frequencies (see Fig. 13 in Paper II for a comparison). For clusters with similar masses (M_{500} ∼

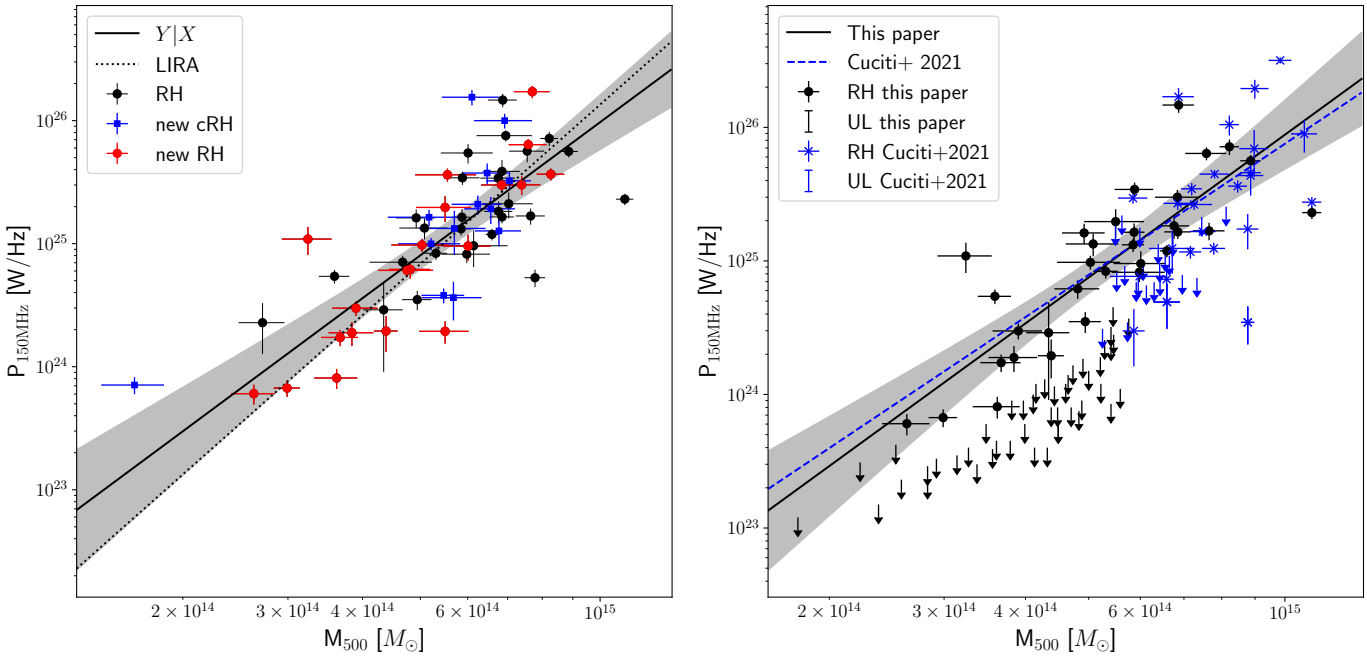

Fig. 6. Comparison with previous studies. Left: black points represent radio halo clusters from the literature, red points are newly discovered radio halos, and blue squares are new candidate radio halos. Right: comparison with Cuciti et al. (2021a) rescaled at 150 MHz assuming $\alpha = -1.3$. Black points and arrows are radio halos and upper limits from the LOFAR sample, and blue stars and arrows are radio halos and upper limits in Cuciti et al. (2021a). The black solid line is the same as in Fig. 2 (right). The dashed blue line is the correlation obtained for the Cuciti et al. (2021a) sample including radio halos and USSRH.

$6 \times 10^{14}\ M_{\odot}$), the upper limits at 150 MHz are typically a factor of 2−5 lower than those at 1.4 GHz (again assuming $\alpha = -1.3$). While at 1.4 GHz, some upper limits below $M_{500} \sim 6.5{\times}10^{14}\ M_{\odot}$ were close to or consistent with the correlation, at 150 MHz this takes place only for $M_{500} < 3 \times 10^{14}\ M_{\odot}$. This suggests the existence of a correlation extending down to masses of at least the order of $M_{500} = 3 \times 10^{14}\ M_{\odot}$.

7. Summary and conclusions

Radio halos are predominantly found in merging systems and their radio power correlates with the mass of their host (e.g. Cassano et al. 2013; Cuciti et al. 2021b). Clusters with undetected radio halos are typically found in non-merging systems and upper limits to the radio power of a possible halo are located below the mass–radio power correlation. Previous statistical studies have mainly been carried out at ∼GHz frequencies, thus limiting our knowledge to the brightest (and massive) objects with intermediate steep spectra ($\alpha \sim -1.3$) only.

In this paper, we analysed the PSZ2 clusters covered by the LoTSS-DR2 (Botteon et al. 2022) with the aim of characterising the distribution of clusters in the M_{500}−$P_{150\,\mathrm{MHz}}$ diagram. We focused on the 221 clusters lying above the 50% *Planck* mass completeness line (Fig. 1). These clusters span wide mass ($3{-}10 \times 10^{14}\ M_{\odot}$) and redshift (0.02−0.6) ranges. Among them, we detected 48 radio halos and 13 candidate radio halos. In addition, we derived upper limits to the radio power of 53 clusters (Paper II).

We confirm the existence of a correlation between the radio power of radio halos and the mass of clusters also at 150 MHz (Fig. 2). We derived the parameters of the correlation with the BCES linear regression algorithms and with the Bayesian method LIRA. We applied these methods to radio halos only, radio halos plus candidate radio halos, and to a subsample of radio halos with $0.06 < z < 0.4$ and $100\,\mathrm{kpc} < r_{\mathrm{e}} < 400\,\mathrm{kpc}$ (Table 2). The parameters of the correlation agree, within the uncertainties, with those found in van Weeren et al. (2021). However, van Weeren et al. (2021) needed to complement the sample with data from the literature in order to reach a sample of 26 confirmed radio halos. Meanwhile, the number of radio halos in this paper is higher by a factor of almost two and the sample selection is much more homogeneous.

The correlation shows a relatively large scatter (Table 2). In the context of turbulent reacceleration models, the scatter of the correlation is expected to increase at low frequency (Cassano 2010), owing to the larger probability of forming radio halos and to the larger fraction of USSRHs. In line with this prediction, we find a hint of increase in the scatter of the correlation at low frequencies (Sect. 6). Similar to the work by Cuciti et al. (2021a) at higher frequencies, we investigated the relation between the scatter of the correlation and the dynamical state of clusters hosting radio halos. To this end, we used the X-ray morphological disturbance, which is a parameter that combines the concentration parameter and the centroid shift, and is commonly used to infer the dynamics of galaxy clusters. We find a clear trend between the distance of radio halos from the correlation and the X-ray morphological disturbance (Fig. 3, right). This indicates that the scatter of the correlation can, at least in part, be attributed to the different merging histories of clusters. This could be due to an increase of either the magnetic field strength or the acceleration efficiency in the most disturbed clusters. The future study of the distribution of radio halo spectra on the mass–radio power diagram will allow us to discriminate between these possibilities. In this respect, the ongoing uGMRT follow up (PI: R. Cassano) of the radio halos belonging to this sample will be crucial to measuring their spectral properties. Although the X-ray information on clusters without radio halos is incomplete, the vast majority of the upper limits are among the less disturbed clusters of the

sample. In order to confirm this, new X-ray observations of clusters without radio halos are required. In this respect, we have obtained (C-priority) *XMM-Newton* observations of the clusters without diffuse emission.

In Sect. 5, we used two approaches to compare the distribution of clusters with and without radio halos in the M_{500}–$P_{150\,\mathrm{MHz}}$ diagram. We used the AIC test to compare two models to fit the radio power. In the first model, both radio halos and upper limits were fitted with the same scaling relation, while in the second one radio halos and upper limits were fitted separately. We find that the latter is the one that best describes the distribution of clusters in the mass–radio power diagram. As a further test, we focused on the distance of clusters from the correlation and implemented a Monte Carlo test to exclude the possibility that the observed bimodal distribution of radio halos and upper limits shown in Fig. 4 is compatible with clusters being uniformly distributed below the correlation. Our test suggests a very low probability that the observed distributions are simply the result of sensitivity limitations applied to a uniform distribution of clusters in the mass–radio power diagram. This needs to be added to evidence that this hypothesis can be firmly excluded for high-mass clusters because all the clusters host radio halos (Fig. 1, right). Our data support the idea of a clear difference in the density of objects from the correlation to the radio-quiet (upper limits) region of the mass–radio power plane. These densities are connected to the amount of time that clusters spend in the different regions of the diagram during their lifetime (see Donnert et al. 2013). Our findings therefore represent an important input for future simulations of particle acceleration in galaxy clusters, which will have to reproduce the journey of clusters through the M_{500}–$P_{150\,\mathrm{MHz}}$ diagram – matching the existence of a correlation – densely populated with radio halo clusters and a much less dense region below the correlation populated by clusters without diffuse emission.

In Fig. 6 (left) we highlight the radio halos, from the clusters used in this paper, that were discovered by LOFAR (Botteon et al. 2022). Of 48 radio halos, 20 are new discoveries, and 10 of these are in low-mass clusters ($M_{500} < 5 \times 10^{14}\,M_{\odot}$), which substantially increases the mass range that can be explored with respect to previous works. In this respect, in Sect. 6, we discussed our statistical findings in comparison with our previous study at higher frequencies (Cuciti et al. 2021a). In spite of the lower statistics available at 1.4 GHz, we show that the correlation found at 150 MHz is in agreement with that derived at 1.4 GHz extrapolated to low frequencies assuming a spectral index of $\alpha = -1.3$ (Fig. 6, right). The number of upper limits and their mass range have also substantially increased with respect to the past (Fig. 6, right). The upper limits obtained with LOFAR are generally deeper than those obtained with the GMRT and this allowed us for the first time to go below $M_{500} \sim 6 \times 10^{14}\,M_{\odot}$ and infer the presence of the correlation down to masses of the order of $M_{500} \sim 3 \times 10^{14}\,M_{\odot}$.

With the completion of LoTSS, we will perform a similar analysis on a sample of clusters that is two to three times larger than the present one, increasing the statistics of radio halos especially at low mass. This will allow us to better constrain the correlation, especially at the low mass end, and the separation between radio halos and upper limits. Indeed, just by extending the Monte Carlo test presented in Sect. 5.2 to the expected number of clusters with radio halos (178) and upper limits (277) in the complete LoTSS (obtained by rescaling the number of radio halos and upper limits in the current sample by the sky coverage), we find that the probability of the clusters being drawn from a uniform distribution below the correlation is <0.1% even with cut = −0.5. This number should only be taken as an indication of the effect of the sample statistics, because its proper assessment requires that the correlation and its scatter be re-evaluated once the survey is completed.

Acknowledgements. We thank the anonymous referee for constructive comments that helped to improve the presentation of our results. V.C. and G.D.G. acknowledge support from the Alexander von Humboldt Foundation. R.Jv.W. acknowledges support from the ERC Starting Grant ClusterWeb 804208. A. Botteon acknowledges support from the ERC-StG DRANOEL n. 714245. A. Bonafede acknowledges support from ERC Stg DRANOEL n. 714245 and MIUR FARE grant "SMS". A.S. is supported by the Women In Science Excel (WISE) programme of the Netherlands Organisation for Scientific Research (NWO), and acknowledges the Kavli IPMU for the continued hospitality. SRON Netherlands Institute for Space Research is supported financially by NWO. R.C., G.B., F.G. and M.R. acknowledge support from INAF mainstream project "Galaxy Clusters Science with LOFAR" 1.05.01.86.05. M.B. acknowledges support from the Deutsche Forschungsgemeinschaft under Germany's Excellence Strategy – EXC 2121 "Quantum Universe" – 390833306. X.Z. acknowledges financial support from the ERC Consolidator Grant DarkQuest No. 101002585. M.S. acknowledges financial contribution from contract ASI-INAF n. 2017-14-H.0. and from contract INAF mainstream project 1.05.01.86.10. LOFAR (van Haarlem et al. 2013) is the LOw Frequency ARray designed and constructed by ASTRON. It has observing, data processing, and data storage facilities in several countries, which are owned by various parties (each with their own funding sources), and are collectively operated by the ILT foundation under a joint scientific policy. The ILT resources have benefitted from the following recent major funding sources: CNRS-INSU, Observatoire de Paris and Université d'Orléans, France; BMBF, MIWF-NRW, MPG, Germany; Science Foundation Ireland (SFI), Department of Business, Enterprise and Innovation (DBEI), Ireland; NWO, The Netherlands; The Science and Technology Facilities Council, UK; Ministry of Science and Higher Education, Poland; Istituto Nazionale di Astrofisica (INAF), Italy. This research made use of the Dutch national e-infrastructure with support of the SURF Cooperative (e-infra 180169) and the LOFAR e-infra group, and of the LOFAR-IT computing infrastructure supported and operated by INAF, and by the Physics Dept. of Turin University (under the agreement with Consorzio Interuniversitario per la Fisica Spaziale) at the C3S Supercomputing Centre, Italy. The Jülich LOFAR Long Term Archive and the German LOFAR network are both coordinated and operated by the Jülich Supercomputing Centre (JSC), and computing resources on the supercomputer JUWELS at JSC were provided by the Gauss Centre for Supercomputing e.V. (grant CHTB00) through the John von Neumann Institute for Computing (NIC). This research made use of the University of Hertfordshire high-performance computing facility and the LOFAR-UK computing facility located at the University of Hertfordshire and supported by STFC [ST/P000096/1]. The scientific results reported in this article are based in part on data obtained from the *Chandra* Data Archive. SRON Netherlands Institute for Space Research is supported financially by the Netherlands Organisation for Scientific Research (NWO).

References

Akaike, H. 1974, IEEE Trans. Autom. Control, 19, 716
Akritas, M. G., & Bershady, M. A. 1996, ApJ, 470, 706
Basu, K. 2012, MNRAS, 421, L112
Böhringer, H., Pratt, G. W., Arnaud, M., et al. 2010, A&A, 514, A32
Bonafede, A., Brunetti, G., Vazza, F., et al. 2021, ApJ, 907, 32
Bonafede, A., Brunetti, G., Rudnick, L., et al. 2022, ApJ, 933, 218
Botteon, A., Shimwell, T. W., Cassano, R., et al. 2022, A&A, 660, A78
Boxelaar, J. M., van Weeren, R. J., & Botteon, A. 2021, Astron. Comput., 35, 100464
Brunetti, G., & Jones, T. W. 2014, Int. J. Mod. Phys. D, 23, 1430007
Brunetti, G., Cassano, R., Dolag, K., & Setti, G. 2009, A&A, 507, 661
Bruno, L., Brunetti, G., Botteon, A., et al. 2023, A&A, 672, A41
Campitiello, M. G., Ettori, S., Lovisari, L., et al. 2022, A&A, 665, A117
Cassano, R. 2010, A&A, 517, A10
Cassano, R., & Brunetti, G. 2005, MNRAS, 357, 1313
Cassano, R., Ettori, S., Giacintucci, S., et al. 2010a, ApJ, 721, L82
Cassano, R., Brunetti, G., Röttgering, H. J. A., & Brüggen, M. 2010b, A&A, 509, A68
Cassano, R., Brunetti, G., Norris, R. P., et al. 2012, A&A, 548, A100
Cassano, R., Ettori, S., Brunetti, G., et al. 2013, ApJ, 777, 141
Cassano, R., Brunetti, G., Giocoli, C., & Ettori, S. 2016, A&A, 593, A81
Cassano, R., Cuciti, V., Brunetti, G., et al. 2023, A&A, 672, A43
Cuciti, V., Cassano, R., Brunetti, G., et al. 2015, A&A, 580, A97
Cuciti, V., Cassano, R., Brunetti, G., et al. 2021a, A&A, 647, A51
Cuciti, V., Cassano, R., Brunetti, G., et al. 2021b, A&A, 647, A50

de Gasperin, F., Williams, W. L., Best, P., et al. 2021, A&A, 648, A104
Donnert, J., Dolag, K., Brunetti, G., & Cassano, R. 2013, MNRAS, 429, 3564
Duchesne, S. W., Johnston-Hollitt, M., Offringa, A. R., et al. 2021, PASA, 38, e010
Feretti, L., Giovannini, G., Govoni, F., & Murgia, M. 2012, A&ARv, 20, 54
George, L. T., Kale, R., & Wadadekar, Y. 2021, MNRAS, 507, 4487
Ghirardini, V., Bahar, Y. E., Bulbul, E., et al. 2022, AAS/High Energy Astrophysics Division, 54, 107.26
Jones, A., de Gasperin, F., Cuciti, V., et al. 2023, A&A, 680, A31 (Paper VI)
Kale, R., Venturi, T., Giacintucci, S., et al. 2013, A&A, 557, A99
Kale, R., Venturi, T., Giacintucci, S., et al. 2015, A&A, 579, A92
Lima, M., & Hu, W. 2005, Phys. Rev. D, 72, 043006
Lovisari, L., Forman, W. R., Jones, C., et al. 2017, ApJ, 846, 51
Murgia, M., Govoni, F., Markevitch, M., et al. 2009, A&A, 499, 679
Planck Collaboration XXVII. 2016, A&A, 594, A27
Rasia, E., Meneghetti, M., & Ettori, S. 2013, Astron. Rev., 8, 40
Santos, J. S., Rosati, P., Tozzi, P., et al. 2008, A&A, 483, 35
Sereno, M. 2016, MNRAS, 455, 2149
Sereno, M., & Ettori, S. 2015, MNRAS, 450, 3675
Shimwell, T. W., Röttgering, H. J. A., Best, P. N., et al. 2017, A&A, 598, A104
Shimwell, T. W., Tasse, C., Hardcastle, M. J., et al. 2019, A&A, 622, A1
Shimwell, T. W., Hardcastle, M. J., Tasse, C., et al. 2022, A&A, 659, A1
van Haarlem, M. P., Wise, M. W., Gunst, A. W., et al. 2013, A&A, 556, A2
van Weeren, R. J., de Gasperin, F., Akamatsu, H., et al. 2019, Space Sci. Rev., 215, 16
van Weeren, R. J., Shimwell, T. W., Botteon, A., et al. 2021, A&A, 651, A115
Venturi, T., Giacintucci, S., Brunetti, G., et al. 2007, A&A, 463, 937
Venturi, T., Giacintucci, S., Dallacasa, D., et al. 2008, A&A, 484, 327
Zhang, X., Simionescu, A., Gastaldello, F., et al. 2023, A&A, 672, A42

Appendix A: Morphological parameter M versus disturbance

Here, we derive the morphological parameter M_C from the combination of c and w using the definition by Campitiello et al. (2022):

$$M_C = \frac{\langle \log c \rangle - \log c}{\sigma_{\log_{10} c}} + \frac{\log w - \langle \log w \rangle}{\sigma_{\log_{10} w}}. \quad \text{(A.1)}$$

With this definition, relaxed systems should have low values of M_C, while disturbed systems should have high values of M_C.

In Fig. A.1 (left), we show the values of the parameter M_C versus the disturbance, as derived in Section 4. We find a well-defined correlation, which indicates that there is good agreement between the two approaches in classifying the dynamical state of clusters. For completeness, we show in Fig. A.1 (right) the distance of radio halos and upper limits (those with available X-ray information) versus the M_C parameter. We confirm the presence of the trend discussed in Section 4 whilst also using this additional parameter.

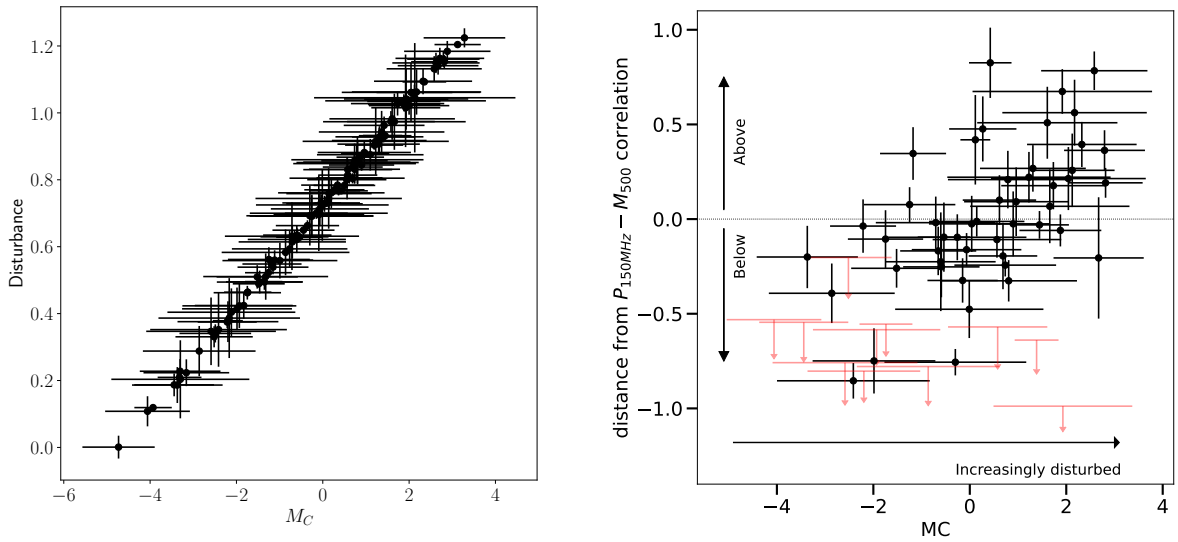

Fig. A.1. Morphological parameter M versus disturbance. Left: Disturbance as derived in Section 4 vs. M. Right: Distance of radio halos from the mass–radio power correlation (BCES Y|X method) vs. M parameter.

Appendix B: Upper limits

Let us consider a variable Y in the domain $Y_{\min} < Y < Y_{\max}$. We assume that Y is a scattered proxy of the variable X, the scatter σ_Y being approximately normal. We can write the probability as

$$p(X, Y) = \frac{1}{\sqrt{2\pi}\sigma_Y} \frac{1}{Y_{\max} - Y_{\min}} \exp\left[-\frac{1}{2}\left(\frac{Y - X}{\sigma_Y}\right)^2\right]. \quad \text{(B.1)}$$

If X is detected whereas Y is not, we can marginalise over Y,

$$p(X) = \frac{1}{2(Y_{\max} - Y_{\min})}\left[\mathrm{erf}\left(\frac{X - Y_{\min}}{\sqrt{2}\sigma_Y}\right) - \mathrm{erf}\left(\frac{X - Y_{\max}}{\sqrt{2}\sigma_Y}\right)\right]. \quad \text{(B.2)}$$

The above expression was used in Eq. (8) for the likelihood of the upper limits.